Iran University of Science and Technology

Enhancing Electric Power Steering Performance: Robust Control Strategies for Noise Suppression and Disturbance Rejection

Pooriya Sanaie[1], Morteza Mollajafari[2*]

[1] Vehicle Electrical and Electronic Research Lab, School of Automotive Engineering, Iran University of Science and Technology, Tehran, Iran

[2] Vehicle Electrical and Electronic Research Lab, School of Automotive Engineering, Iran University of Science and Technology, Tehran, Iran

ARTICLE INFO	A B S T R A C T
	Electric Power Steering (EPS) systems are increasingly being integrated into modern vehicles, offering enhanced fuel efficiency and improved maneuverability. However, these systems are often subject to noise and disturbances, which can significantly impact steering precision and driver comfort. Addressing these challenges requires the implementation of robust control strategies capable of mitigating noise and disturbances in EPS systems. This paper explores advanced methods for achieving robust control in Electric Power Steering systems by reducing noise interference and countering external disturbances. Key techniques involve adaptive control algorithms and robust filtering mechanisms that maintain system stability and performance even under variable operating conditions. Experimental results demonstrate that these robust control approaches effectively minimize noise levels and disturbance impacts, leading to smoother steering response and greater reliability. This study underscores the critical role of robust control in enhancing the functionality and safety of Electric Power Steering systems while highlighting the intricate dynamics between noise, disturbances, and control system robustness in automotive applications.

1. Introduction

Today's ground vehicles are among the most significant examples of electronic control system applications. Over the last two decades, advances in electronics have resulted in the widespread use of electronic control systems in ground vehicles. Automotive control and mechatronics have become essential in improving safety, reducing pollutant emissions, and providing fuel economy

[1]. In Europe, 160 billion euros are lost annually due to accidents, equivalent to 2% of the GNP of Europe. There are 41,000 deaths and a large number of injuries resulting from road vehicle accidents each year [2]. Vehicle control systems, such as electric power steering, are crucial for preventing accidents and reducing fatalities and serious injuries. Examples of control systems applied to passenger vehicles include Anti-lock

Enhancing Electric Power Steering Performance: Robust Control Strategies for Noise Suppression and Disturbance Rejection

Braking System (ABS), Traction Control Systems (TCS), Electronic Stability Control (ESC), Adaptive Cruise Control (ACC), Rollover Avoidance System, Lane Departure Warning, and Lane Keeping Assistance Systems (LDW/LKA), as well as Collision Warning and Collision Avoidance Systems (CW/CA). The design, improvement, and adaptation of new control systems continue at university research labs and automotive companies' R&D centers. Moreover, the use of electric power steering and other vehicle control systems is rapidly increasing. For example, in 1995, only 5% of new cars in Germany were equipped with ESP; by 2004, the proportion in Europe rose to 36%, with even higher rates in some European countries, such as 67% in Germany [3]. Electric Power Steering (EPS) systems have become increasingly prevalent in modern vehicles due to their efficiency and performance benefits. A 2024 study highlights the advantages of EPS, including enhanced steering flexibility and improved vehicle stability [4]. Vehicle control systems, including electric power steering, are essential components of intelligent vehicles and intelligent transportation systems, working alongside sensing and perception technologies. Robust Control of these systems is necessary for ensuring safe and efficient operation, with a focus on objectives and constraints specific to autonomy in vehicles. Today's control systems, such as ACC and LKA, represent initial examples of autonomous behavior, supported by electric power steering for enhanced maneuverability. The development of vehicle control systems, including robust Disturbance Rejection and Noise Suppression techniques, plays a significant role in advancing intelligent autonomous vehicles [5].

In addition to their importance in intelligent vehicles and intelligent transportation systems, control systems for electric vehicles pose unique challenges. There is growing interest in fully electric vehicles within the automotive industry as meeting new and upcoming emission regulations for internal combustion engines becomes more challenging. Consequently, some automotive producers are introducing various fully electric vehicles to the commercial market, while others are building and evaluating research prototypes. Fully electric vehicles, which typically do not have internal combustion engines, are lighter and exhibit different dynamic characteristics compared to their predecessors. As a result, their electronic control systems, including electric power steering, must be redesigned to accommodate these changes [6]. For example, regenerative braking in fully electric vehicles must be considered when designing braking controllers, such as ABS [7].

Despite significant advancements in Electric Power Steering (EPS) systems, existing research has primarily focused on isolated robust control strategies for addressing noise and disturbance challenges. However, these approaches often lack the adaptability and comprehensive validation necessary to handle the complex dynamics of real-world EPS applications. This study introduces a novel integration of parameter-space-based robust control techniques and adaptive disturbance observer methodologies to achieve a more holistic solution.

Our key contributions are as follows:

1. **Innovative Robust Control Design**: A novel robust PI controller framework is developed, utilizing parameter space mapping to ensure stability and performance under significant variations in system parameters and external disturbances.

2. **Enhanced Noise Suppression**: Advanced filtering techniques are implemented, providing measurable improvements in noise reduction and ensuring smoother steering responses even under variable operating conditions.

3. **Comprehensive Validation**: The proposed methodologies are experimentally validated, demonstrating superior robustness, reduced noise levels, and enhanced steering precision compared to conventional techniques.

4. **Practical Impact**: The research bridges critical gaps by addressing both theoretical and practical limitations in EPS systems, offering scalable solutions for improved driver comfort, safety, and reliability.

This work represents a significant advancement in EPS system control, offering a comprehensive approach that outperforms existing methodologies in robustness, adaptability, and real-world application. By addressing persistent challenges in noise suppression and disturbance rejection, the study establishes a strong foundation for future research in intelligent and autonomous vehicle systems.

2. Modeling

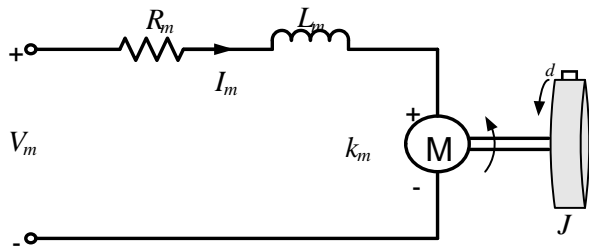This section describes the DC motor modeling. Figure 1 shows the dc motor scheme with its electrical and mechanical parts.

FIGURE 1: DC schematic Motor

Using kirchhoff's law, the following equation is obtained.

$$V_m = L_m \frac{dI_m}{dt} + R_m I_m + K_i W_m \qquad (1)$$

where v_m is the voltage from the amplifier which drives the motor, r_m is the motor armature resistance, i_m is the motor armature current, l_m is the motor armature inductance, k_i is the back- emf constant and ω_m is the motor angular speed [8].

The dynamics of the motor is given by newton's second equation with the following Equation:

$$j\dot{w}_m = K_m I_m + \tau_d \qquad (2)$$

Where j is the total moment of inertia (motor rotor and the load), τ_d is the disturbance torque and k_m is the motor torque constant. In SI units, the motor torque constant is equal to back-EMF constant, that is $k_i = k_m$. After this, k_m is used for both constants.

Using (1) and (2) and assuming $l_m << r_m$ and neglecting the viscous friction in the system, the transfer function $g(s)$ from voltage applied to the motor to motor angular speed can be written as follows:

$$G(s) = \frac{K_m}{R_m \left(JS + \frac{K_m^2}{R_m} \right)} \qquad (3)$$

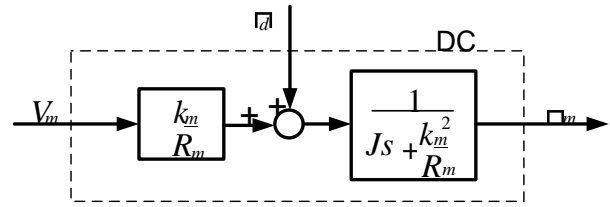The open loop block diagram of the motor with torque disturbance is depicted in figure 2.

FIGURE 2: Open loop block diagram of the dc motor with torque disturbance

In the simulations and experiments with DC motor set which includes a Maxon high quality dc motor is used. The nominal parameters of the dc motor used is given at table 1.

Table 1: The nominal parameters of the dc motor[9].

Parameter	Value	Unit
Km	0.0502	Nm/a
J	22.1×10^{-6}	Kgm^2
Rm	10.6	Ω

Two parameters km and j are taken as uncertain parameters considering $\pm 20\%$ uncertainty on nominal values. Values are between 0.0402 and 0.0602 nm/a and values are between 17.68×10^{-6} and 26.52×10^{-6} kgm^2. An uncertainty box is Depicted in figure 3 for showing these uncertainties[10].
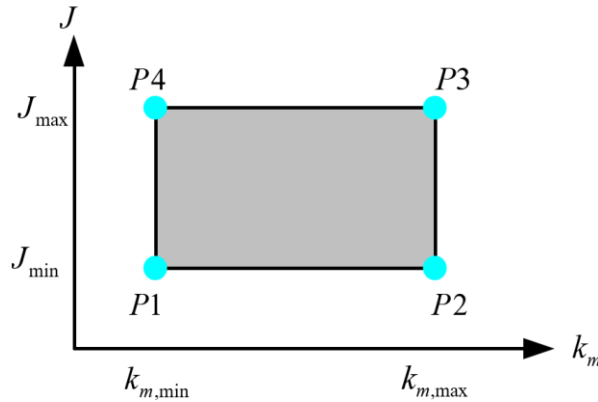
Figure 3: Uncertainty box for the motor parameters

3.Methodology

In this section, a robust PI controller design methodology based on parameter space approach is introduced. The mapping of multi-objective design requirements into the parameter space is explained including Hurwitz stability, d-stability, phase margin bounds and frequency domain (mixed sensitivity) bounds mapping. The PI controlled closed loop system can be seen from figure 4. 3.1 Hurwitz stability

Consider the plant is given by

$$G(s) = \frac{N(s)}{D(s0)} \qquad (4)$$

Where n represents the numerator of the plant and d represents the denominator of the plant. The real and imaginer parts of the numerator and denominator can be defined as:

$$n(j\omega) = n_r(\omega) + jn_i(\omega) \qquad (5)$$

$$d(j\omega) = d_r(\omega) + jd_i(\omega) \qquad (6)$$

The pi controlled closed loop system characteristic equation can be written as

$$P_c(s) = sd(s) + (k_p s + k_i)n(s) = a_{n+1}s^{n+1} + a_n s^n \qquad (7)$$
$$+ \cdots + a_1 s + a_0 = 0$$

Where n is the degree of the plant $g(s)$.

The Hurwitz stability boundary crossed by a pair of complex conjugate roots is characterized by the following equations:

$$Re[p_c(j\omega)] = 0 \qquad (8)$$

$$im[p_c(j\omega)] = 0, \ \forall \omega \in (0,\infty] \qquad (9)$$

this is called as complex root boundary (CRB).

There may be a real root boundary such that a single real root crosses the boundary at frequency $\omega = 0$ is characterized by

$$p_c(0) = 0 \text{ or } a_0 = 0 \qquad (10)$$

This is called as real root boundary (RRB).

There may exists an infinite root boundary (IRB) which is characterized by a degree drop in characteristic polynomial at $\omega = \infty$. This degree
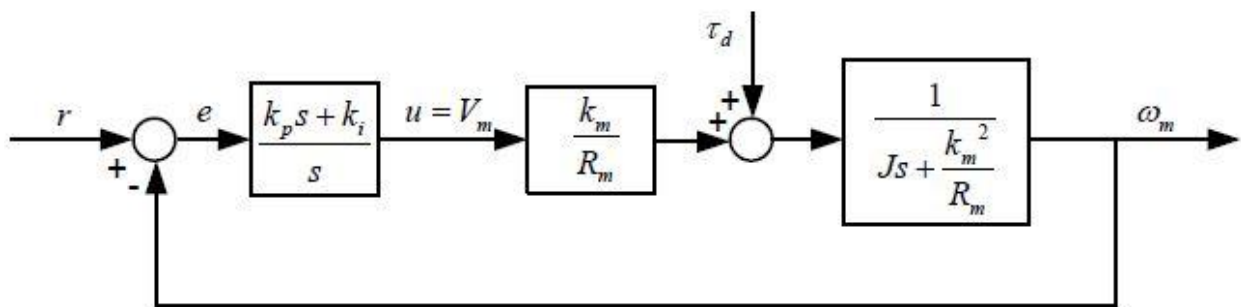

FIGURE 4: PI controlled closed system block diagram

drop in characteristic polynomial is characterized as

$$A_{n+1} = 0 \tag{11}$$

CRB, RRB and IRB solutions by parameterizing ω can be plotted into the $k_p - k_i$ parameter plane to show the Hurwitz stability regions of the given closed loop system. The $k_p - k_i$ values which provide Hurwitz stability can be chosen visually from the stable region of the parameter plane. The aforementioned parameter space computation method to determine Hurwitz stability regions can be extended to specify relative stability regions such as d-stability. A closed loop system is d-stable when the roots of the closed loop characteristic equation lie in the d-stable region in the complex plane as depicted in figure 5. Figure 5 provides critical insights into the stability of the closed-loop system. It demonstrates the impact of varying proportional (K_p) and integral (K_i) gains on system stability. The shaded region represents robust parameter choices, while the boundaries ∂_1, ∂_2, and ∂_3 reflect specific constraints related to root placement, damping characteristics, and disturbance rejection. This analysis supports the design of controllers with enhanced stability and robustness. Note that for $\partial 1$, no Infinite Root Boundary (IRB) exists due to the bounded nature of the d-shaped region.
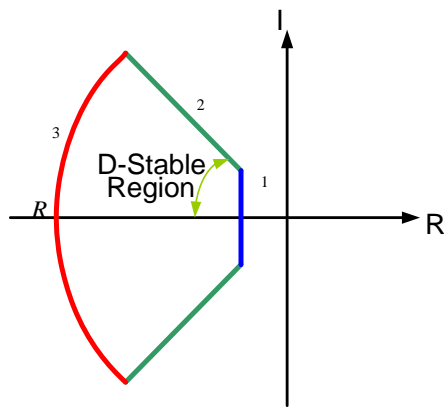

FIGURE 5: The d-stable region in the complex plane showing boundaries $\partial 1$, $\partial 2$, and $\partial 3$

The shaded region indicates stable parameter combinations. This visualization aids in robust controller design by identifying regions where system stability criteria are satisfied, including Hurwitz and d-stability conditions. The boundary ∂_1 in figure 5 can be mapped into the parameter space by using $s - \sigma$ instead of s in (6) in order to shift the stability boundary to ∂_1 in the complex plane. For the $\partial 1$ boundary, the absence of the Infinite Root Boundary (IRB) is a direct consequence of the bounded nature of the d-shaped stability region. In this region, the characteristic polynomial does not exhibit a degree drop at $s \to \infty$ as $s = \infty$ is excluded by construction. This ensures that all roots remain finite and confined within the mapped parameter space. Solving for k_p and k_i in (7) for CRB and (8) for RRB, and then plotting results in the $k_p - k_i$ plane will result in the ∂_1 boundary in the parameter space. For ∂_1 boundary, there is no IRB because s is never equal to infinity in the d-shaped region. For mapping ∂_2 boundary, use $re^{j\theta}$ for s in (6) and parameterize r in $re^{j\theta}$ to obtain the CRB of ∂_2. No RRB and IRB solution exists because r is never equal to zero or infinity. Lastly, ∂_3 boundary maps into the parameter space by substituting s with $re^{j\theta}$ where r is constant and parameterizing over θ in (6). This results in CRB for changing θ and RRB for $\theta = 0$[11].

3.2 ILSC system structure

The proposed ILSC system consists of subsystems such as corrective yaw moment calculation, braking torque distribution algorithm, wheel slip control and torque reduction algorithm. The corrective yaw moment calculation is based on a scheduled LQR controller. The corrective yaw moment actuation is achieved through individual wheel braking. The braking torque distribution algorithm and wheel slip controls are also used at the lower control level. The wheel slip controller is a bang-bang controller where the desired slip ratios are determined based on a scheduled LQR controller.

Enhancing Electric Power Steering Performance: Robust Control Strategies for Noise Suppression and Disturbance Rejection

In addition to the individual braking intervention, electric motor torque reduction is applied when the individual braking is not enough to provide lateral stability of the vehicle. Figure 6 shows the control structure of the proposed ILSC system. The inputs of the vehicle are front wheel steering angle (δ_f), the tire braking pressures (p_{bi}) and the torque reduction command. The outputs of the vehicle are the vehicle side slip angle (β), the vehicle yaw rate (r), the vehicle velocity (v) and individual wheel angular velocities (ω_i). The lateral stability control algorithm needs measurement or estimation of several vehicle variables. For example, yaw rate and wheel angular velocities are easily measured using standard sensors. In contrast, vehicle side slip angle, tire-road friction coefficient and vehicle velocity should be estimated since the measurement of these variables is not economically feasible for commercial road vehicles. Several studies on the estimation of the

aforementioned vehicle parameters is available in the literature [79–82]. The ILSC system, as shown in Figure 6, integrates multiple control subsystems to enhance lateral stability. The corrective yaw moment (M_z) is computed using a Linear Quadratic Regulator (LQR) based on the errors in the vehicle's yaw rate (r) and side-slip angle (β). This moment is then distributed among the individual wheels through a braking torque distribution algorithm. The wheel slip ratios are regulated using a bang-bang control strategy to prevent excessive slip and maintain traction. If individual braking is insufficient, a torque reduction algorithm reduces the electric motor's output torque, ensuring stability under extreme conditions. The combination of these mechanisms allows the ILSC system to provide robust lateral stability across a wide range of operating conditions. The proposed control system structure is shown in figure 6.
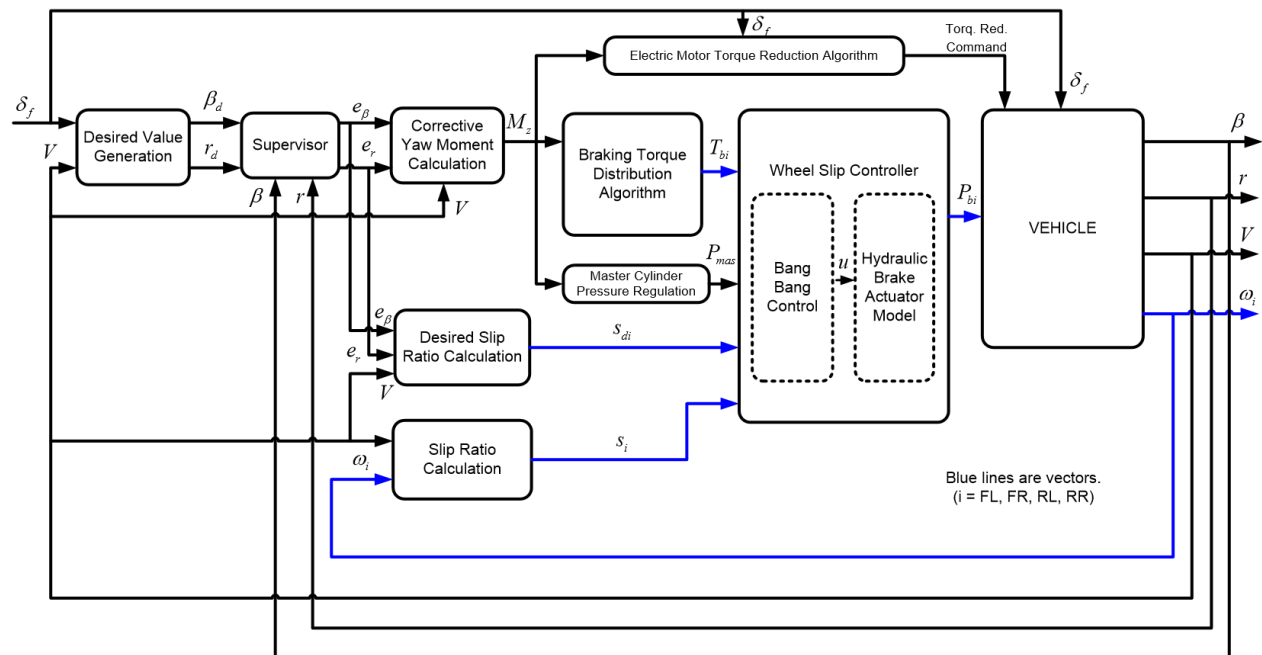

FIGURE 6: Integrated Lateral Stability Control (ILSC) system structure. The algorithm incorporates corrective yaw moment calculation, braking torque distribution, wheel slip control using bang-bang logic, and torque reduction to ensure lateral stability.

In the desired value generation subsystem, the desired values of the vehicle yaw rate and side slip angle are calculated based on current values of steering angle and vehicle velocity. The error values of side slip angle and yaw rate (e_β and e_r, respectively) are determined by the help of the supervisor. The supervisor contains threshold value triggers to prevent the working of the ILSC system when the error of side slip angle and yaw rate are small. Using the error values of side slip angle and yaw rate, the corrective yaw moment is calculated and this corrective yaw moment acts on the vehicle through the braking torque distribution algorithm.The individual wheel slip controllers are used for individual wheel braking. In addition to the individual wheel braking intervention, electric motor torque reduction is applied when the individual braking is not enough to provide lateral stability of the vehicle. The details of these actuations and the subsystems are explained in the following sections[12].

3.3 Disturbance observer structure

The disturbance observer is a well-known approach in the mechatronic systems control area that is used to achieve insensitivity to modeling error and disturbance rejection. It was introduced by [13] and further refined by [14]. It has been used successfully in a variety of mechatronics applications. For instance, friction compensation in [15], road vehicle yaw stability control in [16], robust atomic force microscope control in [17], power assisted electric bicycle control in [18], table drive system in [19] and hard-disc-drive servo system in [20]. In the disturbance observer approach, the inverse of the desired or nominal plant model is used to observe the disturbances and to cancel the effect of disturbances in the control signal. As a result, the closed system is forced to act like its nominal or desired model. The system structure with add-on disturbance observer is depicted in figure 7.

Consider plant g with multiplicative uncertainty Δ_m and input disturbance d:

$$y = g(u+d) \tag{12}$$

Where $g = g_n(1+\Delta_m)$ and g_n is the nominal model of the plant. The aim in the disturbance observer usage is to obtain
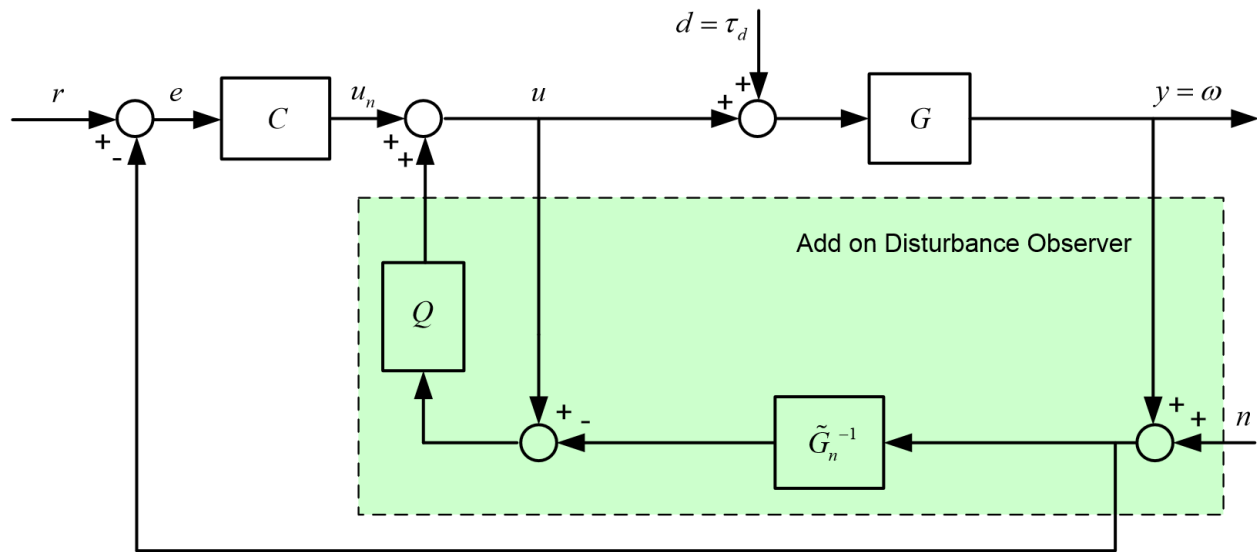

FIGURE 7: system structure with add-on disturbance observer

Enhancing Electric Power Steering Performance: Robust Control Strategies for Noise Suppression and Disturbance Rejection

$$y = g_n u_n \tag{13}$$

Where u_n is the new control input. This aim can be achieved in disturbance observer design by treating the external disturbance and model uncertainty as an extended disturbance e and solving for it as

$$y = G_n u + G_n d + G_n u \Delta_m + G_n d \Delta_m \tag{14}$$

$$e = y - G_n u \tag{15}$$

And using the new control signal u_n given by

$$u = u_n - \frac{1}{G_n} e = u_n - \frac{1}{G_n} y + u \tag{16}$$

To approximately cancel its effect when substituted in (14). With the aim of not to overcompensate at high frequencies and to avoid stability robustness problems, the feedback signals in (16) are multiplied by the low pass filter q. In this case, the final equation becomes:

$$u = u_n - Q \left(\frac{1}{G_n} (y + n) + u \right) \tag{17}$$

Where n represents the sensor noise, it is available for the case of real implementation. The disturbance observer can be designed both in continuous time and discrete time. For discrete time design, please refer to [17]. In discrete time implementation, if g_n (z) is a minimum phase system, its inverse can directly be assigned, if not, stable version of $\tilde{g}_n^{-1}$ (z) can be obtained using input shaping filter (ISF) designing techniques such as zero phase error tracking control (ZPETC), precision tracking control (PTC), optimal precision tracking control (OPTC). The loop gain of the disturbance observer compensated plant is

$$L = \frac{GQ}{G_n(1 - Q)} \tag{18}$$

$$\frac{y}{u_n} = \frac{G_n G}{G_n(1 - Q) + GQ} \tag{19}$$

$$\frac{y}{d} = \frac{1}{1 + L} = \frac{G_n(1 - Q)}{G_n(1 - Q) + GQ} \tag{20}$$

$$\frac{y}{n} = \frac{-L}{1 + L} = \frac{-G_n Q}{G_n(1 - Q) + GQ} \tag{21}$$

It is seen that q must be a unity gain low pass filter. This choice will result in $y/u_n \to g_n$, $y/d \to 0$ at low frequencies where $q \to 1$ and $y/n \to 0$ at high frequencies where $q \to 0$.

There are limitations in the selection of the bandwidth of the q filter. First of all, the bandwidth of the q filter cannot exceed the bandwidth of the actuator used. Another limitation for the q filter arises from the robust stability requirement. The characteristic equation of the disturbance observer compensated system can be written

$$g_n(1-q) + g_n(1+\Delta_m)q = 0 \tag{22}$$

$$g_n(1+\Delta_m)q = 0 \rightarrow Q = -\frac{1}{\Delta m} \tag{23}$$

and note that when the presence of Δ_m does not change the number of unstable poles and zeros of g in comparison to those of g_n, the application of the Nyquist stability criterion results in

$$|Q| < \left| \frac{1}{\Delta_m} \right|, \forall \omega \tag{24}$$

As the necessary and the sufficient condition for robust stability. The feedback controller c also affects the robust stability of the overall system. In the presence of the feedback control as shown in figure 7, the closed loop system, disturbance rejection and sensor noise rejection transfer functions can be written as

$$\frac{y}{r} = \frac{CG_n G}{G_n(1 - Q) + G(CG_n + Q)} \tag{25}$$

$$\frac{y}{d} = \frac{G_n(1 - Q)}{G_n(1 - Q) + G(CG_n + Q)} \tag{26}$$

$$\frac{y}{n} = \frac{-G(CG_n + Q)}{G_n(1 - Q) + G(CG_n + Q)} \qquad (27)$$

In the case of feedback control, the characteristic equation of the closed loop system can be written by

$$G_n(1-q) + g_n(1+\Delta_m)(cg_n + q) = 0 \qquad (28)$$

$$G_n\left(1 + cg_n + \Delta_M(Cg_n + q)\right) =$$
$$0 \to \frac{cg_n + q}{cg_n + 1} = -\frac{1}{\Delta_m} \qquad (29)$$

And using the nyquist stability criterion results in

$$\left|\frac{Cg_n + q}{cg_n + 1}\right| < \left|\frac{1}{\Delta_m}\right|, \forall_\omega \qquad (30)$$

As the necessary and the sufficient condition for robust stability including feedback control shown in figure 7. Thus, robust stability condition of the system can be investigated in the absence and presence of the feedback control using (24) and (30), respectively.

3.4 Disturbance concept

The structure of the communication disturbance observer is similar to the structure of the disturbance observer except the disturbance definition and time delay compensation. The time delayed system is rewritten using the network disturbance concept. The effect of the time delay can be expressed as shown in figure 8 where the time delay is seen as a disturbance that is acting on the system.
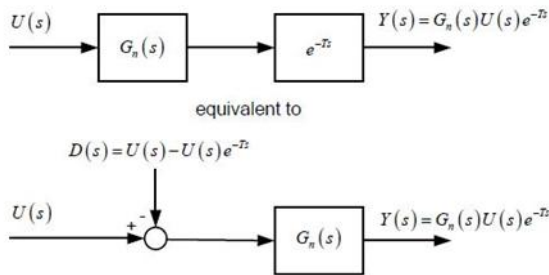

FIGURE 8: network disturbance concept

The network disturbance is defined as follows:

$$D(t) = u(t) - u(t-1) \qquad (31)$$

Or in Laplace form

$$D(s) = u(s) - u(s)e^{-ts} \qquad (32)$$

Where u is the system input and t is the time delay. $D(s)$ is called the network Disturbance.

3.5 Robust stability analysis in the time delay

For an uncertain system, the uncertain plant model $g(s)$ can be represented using multiplicative uncertainty as follows:

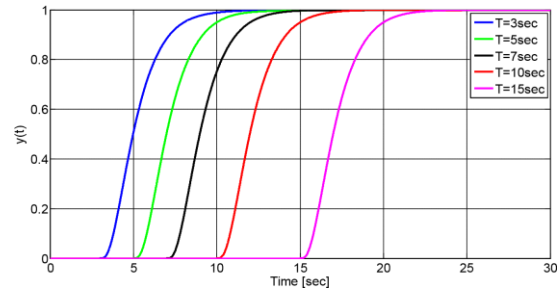$$G(s) = g_n(s)(1+\Delta_m(s)), \forall\omega \qquad (33)$$

FIGURE 9. step responses of the time delayed integral plant for different delay values and for different cutoff frequencies ωc of q(s).

Where $g_n(s)$ is the nominal model and $g(s)$ denotes a family of models that deviate no more than the multiplicative uncertainty $\Delta_m(s)$.

A system with multiplicative uncertainty is depicted in figure 10. For this system, the loop transfer function is written as

$$L = kg = kg_n(1+\Delta_m) = l_n + l_n\Delta_m \qquad (34)$$

Where, k is the controller and $l_n = kg_n$ is the nominal loop transfer function.

If we assume that the nominal closed loop system is stable, robust stability of the uncertain system can be guaranteed if l does not encircle the point

Automotive Science and Engineering (ASE)   4597

Enhancing Electric Power Steering Performance: Robust Control Strategies for Noise Suppression and Disturbance Rejection

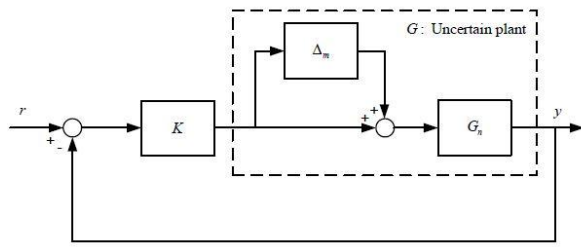(−1,0) according to Nyquist stability criterion. Figure 11 depicts this robust stability condition.

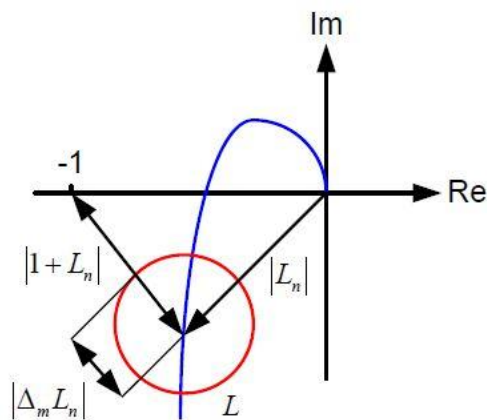**FIGURE 10: Feedback controlled plant with multiplicative uncertainty.**

FIGURE 11: Nyquist plot for illustrating robust stability condition

This condition can be expressed as follows:

$$|\Delta_m(j\omega)l_n(j\omega)| < /1+l_n(j\omega)|, \forall\omega \qquad (35)$$

Or equivalently

$$\left|\frac{\Delta_m(j\omega)L_n(j\omega)}{1+L_n(j\omega)}\right| < 1, \forall\omega \Leftrightarrow \|\Delta_m T_n\|_\infty < 1 \quad (36)$$

Where t_n is the nominal complementary sensitivity function control can be represented as

$$K = \frac{C(1-Q)}{1+CGnQ} \qquad (37)$$

The nominal loop transfer function for the system is written as

$$L_n = KG_n e^{-Ts} = \frac{C(1-Q)G_n e^{-Ts}}{1+CGnQ} \qquad (38)$$

Using (38), the nominal complementary sensitivity function is given by

$$T_n = \frac{L_n}{1+L_n} = \frac{CG_n e^{-Ts}(1-Q)}{1+CG_nQ+CG_n e^{-Ts}(1-Q)} \quad (39)$$

As a result, the robust stability condition in (36) can be written for communication disturbance observer based controlled system as:

$$\left|\frac{CG_n e^{-Ts}(1-Q)}{1+CG_nQ+CG_n e^{-Ts}(1-Q)}\right|\left|\frac{1}{\Delta_m}\right|, \forall_\omega (40)$$

To illustrate the effects of time delay, assume that e^{-ts} is the only source of unmodeled dynamics. Thus, the multiplicative uncertainty model can be represented as

$$\Delta_m(s) = e^{-ts} - 1 \qquad (41)$$

Consider the following time delayed basic integral plant for robust stability analysis:

$$G_p(s) = \frac{1}{s}e^{-ts} \qquad (42)$$

The nominal model G_n is equal to $\frac{1}{s}$. The time delay t is taken as 0.2 seconds. The controller C(s) is a proportional controller, set to 20 to ensure a short settling time and no overshoot, as per design requirements. The robust stability condition (40) is analyzed for different cut-off frequencies of q(s). It is observed that the uncertainty and robust stability lines intersect at ω_c=10 rad/sec. At this frequency, the feedback-controlled integral plant may become unstable. For other cut-off frequency values, the system remains stable. Increasing the cut-off frequency enhances the stability margin. However, in real applications, noise concerns may limit the selection of this frequency.

3.6 Robust PID steering control in parameter space for highly automated driving

In recent years, intelligent vehicle systems and highly automated driving technologies have drawn interest among researchers. Many research efforts, including for example the work of [21, 22], have concentrated on semi-autonomous and fully autonomous vehicles. Autonomous driving requires the coordinated automation of the longitudinal and lateral driving tasks of speed control and steering control, respectively. Desired path tracking of an autonomous vehicle requires the proper design and implementation of steering and speed controllers at the lower control level. This section concentrates on automated robust steering control. The basic automatic steering control algorithms found in the literature are based on proportional-type controllers [23]. In these designs, the lateral deviation of the vehicle at a preview distance is fed back for controlling the vehicle's lateral dynamics. In [24], a robust PID controller is designed for automatic bus steering control as a solution to a benchmark problem. The yaw rate is measured in addition to lateral deviation measurements and is fed back to improve control system performance. For the same benchmark problem, a discrete-time add-on disturbance observer design is realized in [16]. Using the add-on disturbance observer, performance improvement is achieved without the need for yaw rate feedback. Another approach to automatic steering controllers is to design nested PI and PID controllers. A PI steering controller that reduces yaw rate tracking error is used to improve vehicle steering dynamics, and a PID controller is employed to reject lateral deviation from the desired path due to road curvature disturbances in [25]. In this section, the parameter space approach-based PID controller design is applied to robust automatic steering control, including considerations for electric power steering systems, which enhance steering responsiveness and efficiency. The theoretical background on the parameter space approach and an example of road vehicle yaw stability control can be found in references [9], [14], and [18]. The parameters exhibiting the largest variation in automatic steering control are taken as uncertain parameters, including vehicle mass, vehicle velocity, and tire-road friction coefficient. In this section, the controller parameter space is obtained by considering d-stability requirements for the two free coefficients of a PID controller, chosen as the proportional gain and the derivative gain . An overall solution region is calculated by intersecting solution regions for exemplary points chosen from the boundary of the uncertain range of parameters. Robust PID coefficients satisfying d-stability are chosen from the overall calculated parameter space regions. The designed controller is applied to an experimentally validated nonlinear dynamics simulation model of a sedan vehicle.

Additionally, robust PID automatic steering control system design is realized based on the digital map and GPS measurements. In this structure, the lateral deviation from the desired path at the preview distance is calculated by comparing the generated map and the vehicle position in real time. High-resolution digital map generation using the constrained least square method is introduced. The proposed control system is tested with the validated nonlinear dynamics vehicle model on a specific eight-segment desired path. The organization of the rest of this section is as follows: The nonlinear dynamics vehicle model used in the controller design and the experimental vehicle that it is based on are described. The nonlinear dynamics model of this experimental vehicle and model validation results are also presented. Robust PID controller design based on mapping d-stability boundaries into parameter space is given in the simulation section.

3.7 Vehicle models and model validation

the vehicle steering behavior is modeled as single track model that also includes the dynamics of following the reference path as illustrated in figure 12.
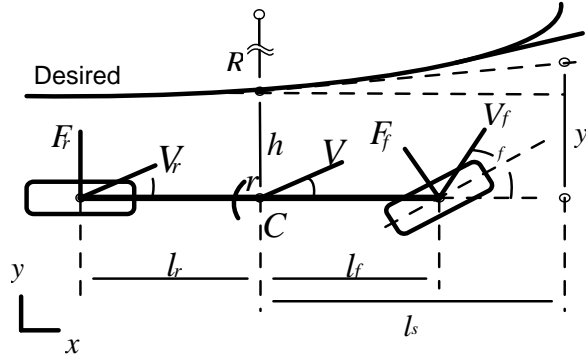
Figure 12: Vehicle steering model

The nonlinear dynamics vehicle steering model is described in state-space form as

$$\begin{bmatrix} \dot{\beta} \\ \dot{r} \\ \Delta\dot{\psi} \end{bmatrix} = \begin{bmatrix} a_{11} & a_{12} & 0 & 0 \\ a_{21} & a_{22} & 0 & 0 \\ 0 & 1 & 0 & 0 \end{bmatrix} \begin{bmatrix} \beta \\ r \\ \Delta\psi \end{bmatrix}$$
$$+ \begin{bmatrix} b_{11} & 0 \\ b_{21} & 0 \\ 0 & -V \end{bmatrix} \begin{bmatrix} \delta_f \\ \rho_{ref} \end{bmatrix} \quad (43)$$

Where β, r, v, $\Delta\psi$, l_s and y are vehicle side slip angle, vehicle yaw rate, vehicle velocity, yaw angle relative to the desired path's tangent, the preview distance and lateral deviation from the desired path at the preview distance, respectively. The control input is the steering angle δ_f. $P_{ref} = 1/r$ is the road curvature where r is the road radius. The remaining terms are

$$a_{11} = \frac{-(c_r + c_f)}{\breve{m}V} \quad (43)$$

$$a_{12} = \frac{1 + (c_r l_r - c_f l_f)}{\breve{m}V^2} \quad (44)$$

$$a_{21} = \frac{(c_r l_r - c_f l_f)}{\breve{J}} \quad (45)$$

$$b_{11} = \frac{c_f}{\breve{m}V} \quad (46)$$

$$b_{12} = \frac{c_f l_f}{\breve{J}} \quad (47)$$

where $\breve{m} = m/\mu$ is the virtual mass, $\breve{J} = J/\mu$ is the virtual moment of inertia, μ is the tire-road

friction coefficient, m is the vehicle mass, j is the moment of inertia, cf and cr are the cornering stiffnesses, lf is the distance from the center of gravity of the vehicle (cg) to the front axle and lr is the distance from the cg to the rear axle [26]. The values of the parameters used are j = 2392 kgm2, lf = 1.07 m, lr = 1.53 m , ls = 2 m, cf = 72463 n/rad and cr = 92492 n/rad. The vehicle mass, the vehicle velocity and the tire-road friction coefficient are taken as uncertain parameters within the ranges of m ∈ [1400,1700] (kg) (the nominal value of mass is 1550 kg), μ ∈ [0.5,1],v ∈ [1,20] (m/s), respectively. The virtual mass, then, is within the range m˘. The corresponding uncertainty box of virtual mass and vehicle speed is illustrated in figure 13.
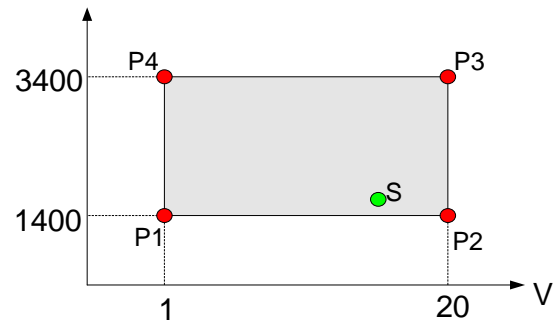

Figure 13: uncertainty box

3.7.1 Nonlinear dynamics vehicle model

The equations of motion for longitudinal and lateral dynamics of the nonlinear dynamics vehicle model are

$$m(a_x - rV_y) = \sum_{i=f,r} F_{xi}\cos\delta_i - F_{yi}\sin\delta_i \quad (48)$$
$$- (F_{aero} + F_{rr} + F_{hc})$$

$$m(a_y - rV_x) = \sum_{i=f,r} F_{xi}\sin\delta_i + F_{yi}\cos\delta_i \quad (49)$$

While the equation of motion around the yaw axis is

$$I_z \dot{r} = I_f F_{yf} cos\delta_f - I_r F_{yr} cos\delta_r$$
$$+ I_f F_{xf} sin\delta_f - I_r F_{xf} sin\delta_r \qquad (50)$$

and f_{yi} are the longitudinal and the lateral tire forces. F and r represent the front and rear tires. A_x, a_y, v_x, v_y and i_z are the longitudinal acceleration at the cg, the lateral acceleration at the cg, the longitudinal velocity at the cg, the lateral velocity at the cg and the moment of inertia about the yaw axis, respectively. Note that the front wheel steered vehicle considered in this section so that the rear wheel steering angle is taken as zero ($\delta_r = 0$) [27]. The resistive forces which affect the longitudinal dynamics of the vehicle are shown in figure 12. The aerodynamic drag force f_{aero} is given by

$$F_{aero} = \frac{1}{2} A p C_d V^2 \qquad (51)$$

Where a is the effective frontal area of the vehicle, ρ is the mass density of air, c_d is the drag coefficient, and v is the velocity of the vehicle. The rolling resistance force f_{rr} is determined as

$$F_{rr} = C_{rr} mgcos(\theta) \qquad (52)$$

where c_{rr} is the rolling resistance coefficient and θ is the road inclination angle. The gravitational slope resistance force f_{hc} is modeled as
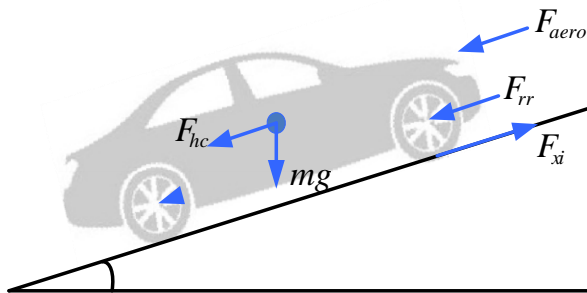
$$F_{hc} = mgcos(\theta) \qquad (53)$$

FIGURE 14: Resistive forces acting on the longitudinal dynamics of the vehicle

The internal combustion engine (ice) is modeled using a static engine map that defines the relationship between the inputs of throttle position α, the engine speed ω and the output engine torque tice(ω,α). The engine torque output is transmitted to the wheels through the driveline as torque td according to

$$T_d = \eta_i i_t T_{ice}(\omega, \alpha) \qquad (54)$$

Where η_i is a static efficiency factor used to model mechanical losses and it is the transmission ratio. These parameters are used to model the transmission of the vehicle. The forces and torques acting on the wheel are shown in figure 15
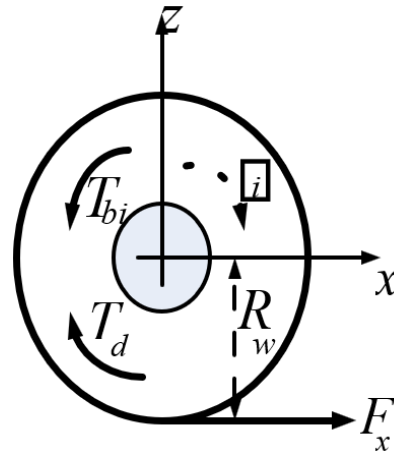
FIGURE 15: forces and the torques acting on the wheel

The moment balance at the center of the wheel is given by

$$I_w \dot{\omega}_i = t_d - t_{bi} - f_{xi} r_w \qquad (55)$$

where i_w is the moment of inertia of the wheel, ω_i is the angular velocity of the ith wheel, t_{bi} is the braking torque on the ith wheel applied through the brake system, f_{xi} is the longitudinal tire force of the ith wheel and r_w is the effective wheel radius. The longitudinal velocities of the front and rear wheels can be determined as follows:

$$V_{fx} = \sqrt{V_x^2 + (V_y + l_f r)^2} \cos\alpha_f \qquad (56)$$

$$V_{rx} = \sqrt{V_x^2 + (V_y - l_f r)^2} \cos\alpha_r \qquad (57)$$

Where the tire slip angles are

$$\alpha_f = \delta_f - \arctan\left(tan\beta + \frac{l_f r}{V_x}\right) \qquad (58)$$

$$\alpha_f = \delta_f - \arctan\left(tan\beta + \frac{l_f r}{V_x}\right) \qquad (59)$$

The longitudinal wheel slip ratio is defined as

$$S_i$$

$$= \begin{cases} \dfrac{R_w w_i - V_{ix}}{V_{ix}}, & R_w w_i < V_{ix}(\text{braking}) \\ \dfrac{R_w w_i - V_{ix}}{R_w w_i}, & R_w w_i \geq V_{ix}(\text{traction}); \\ & (\text{i} = \text{f}, \text{r}) \end{cases}$$

$$(60)$$

The Dugoff Wheel model is used for the calculations of the tire forces as

$$F_{xi} = f_i C_{xi} S_i \qquad (61)$$

$$F_{yi} = f_i C_{yi} \alpha_i \qquad (62)$$

Where c_{xi} and c_{yi} are the longitudinal and the lateral cornering stiffness of the ith wheel. The coefficients f_i are determined using

$$f_i = \begin{cases} 1, & F_{Ri} < \dfrac{\mu F_{zi}}{2} \\ (2 - \dfrac{\mu F_{zi}}{2F_{Ri}})\dfrac{\mu F_{zi}}{2F_{Ri}}, & F_{Ri} \geq \dfrac{\mu F_{zi}}{2} \end{cases} \qquad (63)$$

$$F_{Ri} = \sqrt{(C_{xi} S_i)^2 + \left(C_{yi} \alpha_i\right)^2} \qquad (64)$$

3.8 Lateral deviation and yaw angle error calculations

The desired trajectory for the robust steering control can be described by the generated digital map. The lateral deviation and yaw angle error of

the vehicle for each segment can be found by comparing the desired trajectory (the generated map) and the vehicle position in real time. Assuming that the radius of the curvature for each segment is large compared to the lateral deviation of the vehicle, the shortest distance from the vehicle to the path is perpendicular with the path tangent. Using vectorial relation shown im figure 16, the dot product between the vehicle's position relative to the path and the slope of the map should be zero to obtain the shortest distance. This dot product can be written as follows:

$$\left((X(\lambda) - P_E), (Y(\lambda) - P_N)\right)\left(\dot{X}(\lambda), \dot{Y}(\lambda)\right) = 0 \quad (65)$$

Where p_e and p_n denote the vehicle's east and north position according to the map Coordinate system, respectively.
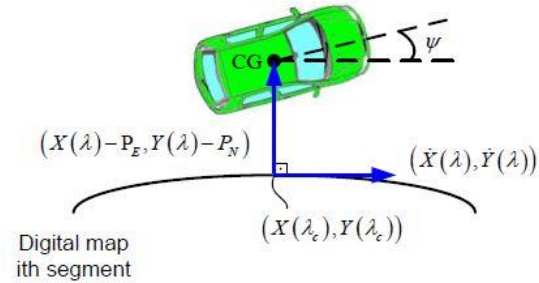

FIGURE 16: lateral deviation and yaw angle error calculations

If the polynomial used to define the map segment is nth order, this dot product polynomial is the order of $2n - 1$. The dot product given in (59) is solved for the distance down the segment, λ_c, which corresponds to the point on the segment closest to the vehicle. Note that the problem given in (59) can be solved for λ_c by a polynomial root-finding algorithm such as matlab's fzero algorithm. Once λ_c is found, it is used to find the distance (the lateral deviation of the vehicle, h) between vehicle's cg and the point on the path identified by λ_c. The lateral deviation of the vehicle, h can be calculated as follows:

$$h = \rho\sqrt{(X(\lambda c) - PE)^2 + (Y(\lambda c) - PN)^2} \quad (66)$$

Where:

$$\rho = \text{sgn}\left(\vec{U}(3)\right) \qquad (67)$$

$$\vec{U} = \left((X(\lambda_c) - P_E), (Y(\lambda_c) - P_N), 0\right) \\ \times \left(\dot{X}(\lambda_c), \dot{Y}(\lambda_c), 0\right) \qquad (68)$$

The ρ is used to determine sign of the lateral deviation of h. It is calculated based on the cross product of the vectors between the vehicle's position relative to the path and the slope of the map. The third dimension of this product gives the direction information of the lateral deviation, h. If h is positive, it means the vehicle is outer of a closed map and if h is negative, the vehicle is inner of a closed map.

Similarly, the yaw angle of the vehicle can be calculated comparing the yaw angle of the vehicle and the slope of the path at the point λ_c.

$$\Delta\psi = \psi - \frac{\dot{Y}(\lambda_c)}{\dot{X}(\lambda_c)} \qquad (69)$$

As a result, using the h and $\Delta\psi$, the lateral deviation y at the preview distance l_s is calculated and this signal is feedback to the controller to maintain robust steering control. The segment switching is also a problem to be solved in this approach. In order to determine when the vehicle switches the segment, an added algorithm checks the distance between the vehicle and the upcoming segment's boundary, if the distance is lower than a predefined distance (for example 1 m), it is assumed that the vehicle switched the segment. Also, it is assumed that the vehicle is always moving forward to maintain consistency.

4.Simulation results

The simulation study is performed to test the digital map and gps measurements based robust pid steering controller for highly automated driving. In the simulation, the vehicle mass and the tire-road friction coefficient are taken as 1500 kg and 1, respectively. The vehicle tries to follow the eight segments desired map with the constant velocity of 15 m/s. The lateral deviation (h) and the yaw angle error ($\Delta\psi$) are calculated following the procedure given in lateral deviation and yaw angle error calculations. After the determination of h and $\Delta\psi$, the lateral deviation y at the preview distance l_s is calculated using these variables. Then, y is used in the feedback controller. Figure 17 shows the desired map and the stroboscopic vehicle trajectory. The vehicle starts its movement from the point (430 m, 240 m) near the segment 1 with 45 degrees initial yaw angle. Firstly the vehicle moves to compensate the distance difference from the segment 1 and then tracks the segment 1 and the upcoming segments successfully.
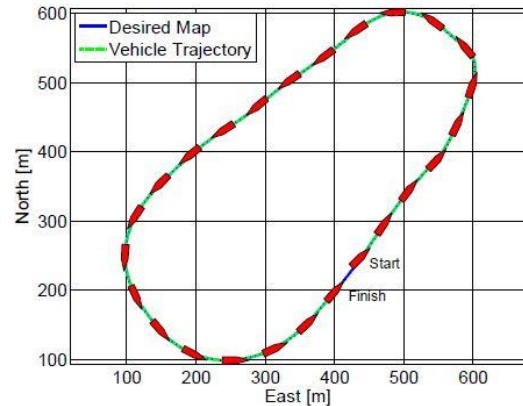

FIGURE 17: Desired map and stroboscopic vehicle trajectory

Figure 18 shows the changes of the segments, the lateral deviation y from the desired path at the preview distance, vehicle velocity v and the vehicle yaw rate r in the simulation. The vehicle tracks the segments from one to eight. It is seen that the lateral deviation at the preview distance is around zero after the settling of the vehicle to the segment 1. The velocity of the vehicle is kept constant at 15 m/s along the path successfully by the pi-based cruise controller. Also, the vehicle yaw rate is at acceptable values during the simulation.

Enhancing Electric Power Steering Performance: Robust Control Strategies for Noise Suppression and Disturbance Rejection

5.Conclusions

A parameter-space-based Robust PID steering controller design for automated steering was developed and tested in a simulation environment in this section. The vehicle mass, vehicle velocity, and tire-road friction coefficient were taken as uncertain parameters in the parameter space design. A validated nonlinear dynamics model of a mid-sized sedan was used in the simulations. In the simulations, the vehicle with uncertain parameters successfully followed different road curvatures with constant and time-varying tire-road friction coefficients. Electric power steering, a critical component for improving steering responsiveness, was integrated into the simulations to evaluate its interaction with the proposed controllers.

Also, Robust PID steering control was performed based on digital map and GPS measurements in this section. This control structure incorporated Disturbance Rejection to ensure that lateral deviation and yaw angle errors were minimized, thereby improving vehicle tracking accuracy. By comparing the desired trajectory and the vehicle position in real time, the system achieved enhanced Noise Suppression. The desired trajectory (the digital map) was calculated using the constrained least squares method. An eight-segment high-resolution digital map was tracked by the validated nonlinear dynamics vehicle model with a high degree of accuracy, demonstrating the effectiveness of Robust Control methods.

The ILSC and RB-LSC systems were presented in this section to improve the lateral stability of a fully electric vehicle. The effectiveness of the proposed control systems was verified through realistic CarSim simulations using a validated model of a fully electric light vehicle, which incorporated electric power steering for enhanced maneuverability. Several simulation studies were conducted, including a sine-with-dwell maneuver and a fishhook test to evaluate the proposed systems. According to these simulations, the
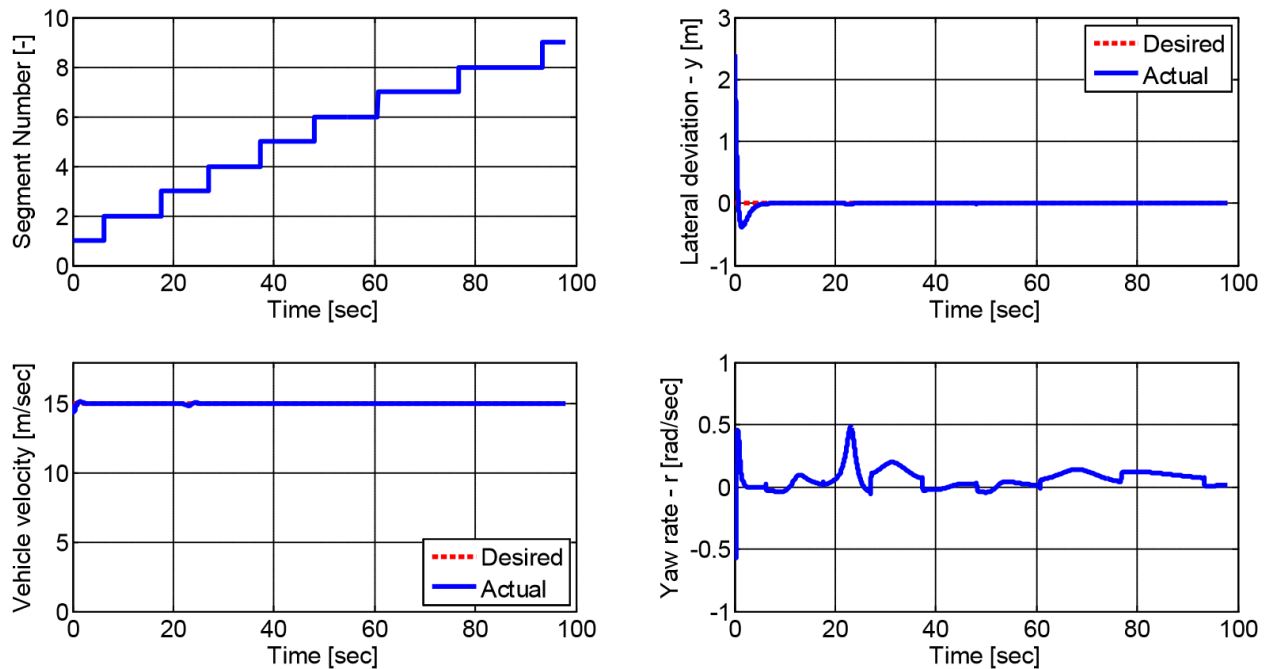

FIGURE 18 changes of important variables

lateral stability of the electric vehicle was significantly improved by using the ILSC system. The results showed superior performance in terms of yaw rate and side-slip angle compared to the basic ESC system. Robust Control strategies were applied to stabilize unstable vehicle behavior using simpler RB-LSC approaches, which, despite their relatively lower performance compared to ILSC, offered a cost-effective means of achieving stability.

This research discusses advanced control methods for ground vehicles, emphasizing Robust Control, Disturbance Rejection, and Noise Suppression as essential features in control system design. The parameter-space-based Robust Control methodology was applied to DC motor speed control, showcasing improved tracking and Disturbance Rejection through the use of an add-on disturbance observer. The designed system demonstrated enhanced Noise Suppression, ensuring stable performance across various disturbances. Three different experiments—trajectory tracking, step Disturbance Rejection, and ramp Disturbance Rejection—highlighted the system's superior robustness.

A novel robust stability condition for handling constant and time-varying delays was established, enhancing Disturbance Rejection capabilities. This condition was applied to the vehicle yaw stability control problem over CAN bus networks, where network-induced delays could compromise system performance. Using electric power steering and the proposed communication Disturbance Observer, time-varying delay issues were mitigated, ensuring robust yaw stability control and improved tracking performance. Robust Control was further demonstrated through the integration of these advanced methodologies in automatic steering systems for autonomous vehicles, employing digital maps and real-time GPS data.

In addition to automated steering control, robust lateral stability control was examined for fully electric vehicles. Two novel control systems were proposed to maintain the desired vehicle side-slip angle and yaw rate, ensuring optimal lateral stability. The integration of electric power steering and Disturbance Rejection mechanisms allowed for precise maneuvering and Noise Suppression during critical driving scenarios. Simulation tests, including sine-with-dwell and fishhook maneuvers, confirmed the efficacy of these systems. Future extensions to this work include applying fractional-order filters for improved Noise Suppression, enhancing the robustness of Disturbance Observer designs, and exploring the use of Robust H∞ control methods for fully electric vehicle stability control.

References

[1]Roy, A., & Pramanik, S. (2024). A review of the hydrogen fuel path to emission reduction in the surface transport industry. *International Journal of Hydrogen Energy*, *49*, 792-821.

[2]Alkaabi, K. (2023). Identification of hotspot areas for traffic accidents and analyzing drivers' behaviors and road accidents. *Transportation research interdisciplinary perspectives*, *22*, 100929.

[3]Shojaeefard, M.H., Mollajafari, M., Ebrahimi-Nejad, S. and Tayebi, S., 2023. Weather-aware fuzzy adaptive cruise control: Dynamic reference signal design. Computers and Electrical Engineering, 110, p.108903.

[4]Li Sanaie, P. and Mollajafari, M., 2024. Designing a disturbance estimator for electric power steering robust controller. Mechanical Engineering for Society and Industry, 4(2).

[5]Bathla, G., Bhadane, K., Singh, R. K., Kumar, R., Aluvalu, R., Krishnamurthi, R., ... & Basheer, S. (2022). Autonomous vehicles and intelligent automation: Applications, challenges, and

opportunities. *Mobile Information Systems*, *2022*(1), 7632892.

[6] Fioriti, M., & Di Fede, F. (2023). A Design Model for Electric Environmental Control System in Aircraft Conceptual and Preliminary Design. *INTERNATIONAL REVIEW OF AEROSPACE ENGINEERING*.

[7] Lupberger, S., Degel, W., Odenthal, D., & Bajcinca, N. (2021). Nonlinear control design for regenerative and hybrid antilock braking in electric vehicles. *IEEE transactions on control systems technology*, *30*(4), 1375-1389.

[8] Okoro, I. S., & Enwerem, C. (2019). Performance assessment of a model-based DC motor scheme. *Applications of modelling and simulation*, *3*(3), 145-153.

[9] Lv, C., Wang, B., Chen, J., Zhang, R., Dong, H., & Wan, S. (2024). Research on a Torque Ripple Suppression Method of Fuzzy Active Disturbance Rejection Control for a Permanent Magnet Synchronous Motor. *Electronics*, *13*(7), 1280.

[10] Rehme, M. F., John, D. N., Schick, M., & Pflüger, D. (2023). Uncertainty Quantification for parameter estimation of an industrial electric motor using hierarchical Bayesian inversion. *Mechatronics*, *92*, 102989.

[11] Oaxaca-Adams, G., Villafuerte-Segura, R., & Aguirre-Hernández, B. (2024). On Hurwitz stability for families of polynomials. *International Journal of Robust and Nonlinear Control*, *34*(7), 4576-4594.

[12] Zhao, F., An, J., Chen, Q., & Li, Y. (2024). Integrated Path Following and Lateral Stability Control of Distributed Drive Autonomous Unmanned Vehicle. *World Electric Vehicle Journal*, *15*(3), 122.

[13] Chen, Y. C., & Woolsey, C. A. (2023). A Structure-Inspired Disturbance Observer for Finite-Dimensional Mechanical Systems. *IEEE Transactions on Control Systems Technology*.

[14] Han, J. W., Park, D., & Kim, M. J. (2024, May). Constrained nonlinear disturbance observer for robotic systems. In *2024 IEEE International Conference on Robotics and Automation (ICRA)* (pp. 3526-3532). IEEE.

[15] Huang, S., Liang, W., & Tan, K. K. (2019). Intelligent friction compensation: A review. *IEEE/Asme Transactions On Mechatronics*, *24*(4), 1763-1774.

[16] Tang, M., Zhang, Y., Wang, W., An, B., & Yan, Y. (2024, March). Yaw Stability Control of Unmanned Emergency Supplies Transportation Vehicle Considering Two-Layer Model Predictive Control. In *Actuators* (Vol. 13, No. 3, p. 103). MDPI.

[17] Keighobadi, J., Hosseini-Pishrobat, M., Faraji, J., Oveisi, A., & Nestorović, T. (2019). Robust nonlinear control of atomic force microscope via immersion and invariance. *International Journal of Robust and Nonlinear Control*, *29*(4), 1031-1050.

[18] Uyar, O., Çunkaş, M., & Karaca, H. (2022). Enhanced intelligent control with adaptive system for electrically assisted bicycle. *Engineering Science and Technology, an International Journal*, *30*, 101047.

[19] Reda, M., Onsy, A., Haikal, A. Y., & Ghanbari, A. (2024). Path planning algorithms in the autonomous driving system: A comprehensive review. *Robotics and Autonomous Systems*, *174*, 104630.

[20] Haas, A., Schrage, B., Menze, G., Sieberg, P. M., & Schramm, D. (2023, April). Improvements on the dynamical behavior of a hil-steering system test bench. In *Actuators* (Vol. 12, No. 5, p. 186). MDPI.

[21] Shojaeefard, M.H., Mollajafari, M., Mousavitabar, S.H.R., Khordehbinan, M.W. and Hosseinalibeiki, H., 2022. A TSP-based nested clustering approach to solve multi-depot heterogeneous fleet routing problem. Métodos numéricos para cálculo y diseño en ingeniería: Revista internacional, 38(1), pp.1-11.

[22] Mesdaghi, A. and Mollajafari, M., 2024. Improve performance and energy efficiency of plug-in fuel cell vehicles

using connected cars with V2V communication. Energy Conversion and Management, 306, p.118296.

[23] P. Sanaie, M. Mollajafari, "Designing a disturbance estimator for electric power steering robust controller," Mechanical Engineering for Society and Industry, Vol. 4, No. 2, 2024. https://doi.org/10.31603/mesi.12650.

[24] Liu, Y., Zong, C., & Zhang, D. (2019). Lateral control system for vehicle platoon considering vehicle dynamic characteristics. *IET intelligent transport systems*, *13*(9), 1356-1364.

[25] Deng, Y., Wang, Y., Wang, H., & Member, Z. Z. (2024). Model Predictive Path-Following Control for UGVs with Curvature Inaccuracy: A Disturbance Rejection Approach Combining Speed Regulation. *IEEE Transactions on Intelligent Vehicles*.

[26] Balaga, S. R., & Singh, K. B. (2024). *Real-Time Cornering Stiffness Estimation and Road Friction State Classification under Normal Driving Conditions* (No. 2024-01-2650). SAE Technical Paper.

[27] Chen, C., Zhang, J., & Zheng, H. (2024). A modified handling stability control strategy for steer-by-wire vehicles based on variable steering ratio and active front steering control. *Proceedings of the Institution of Mechanical Engineers, Part D: Journal of Automobile Engineering*, 09544070241261113